JGR Space Physics

RESEARCH ARTICLE
10.1029/2019JA026751

A Self-Regulating Equilibrium Magnetopause Model With Applications to Saturn

F. Hardy[1,2], N. Achilleos[1,2], and P. Guio[1,2]

[1]Department of Physics and Astronomy, University College London, London, UK, [2]Centre for Planetary Sciences at UCL/Birkbeck, London, UK

Key Points:
- We construct a reference model of a planetary magnetopause based on pressure equilibrium
- We explain how the model provides realistic boundary features produced by the assumed structure of the magnetic field inside the boundary
- We describe cases of a pure dipole field, pure dipole field plus plasma pressure, and dipole plus plasma pressure and ring currents

Correspondence to:
F. Hardy,
flavien.hardy.17@ucl.ac.uk

Citation:
Hardy, F., Achilleos, N., & Guio, P. (2019). A self-regulating equilibrium magnetopause model with applications to Saturn. *Journal of Geophysical Research: Space Physics*, *124*. https://doi.org/10.1029/2019JA026751

Received 29 MAR 2019
Accepted 27 JUN 2019
Accepted article online 12 AUG 2019

Abstract We describe a new method of constructing an equilibrium magnetopause surface based on the pressure balance between external and internal pressure sources. Details are given for every step of the procedure, including the initial pressure balance condition (which determines magnetopause morphology), the related underlying assumptions, and the final optimized magnetopause surface. Our method produces a final equilibrium magnetopause surface that satisfies the local balance between the solar wind dynamic pressure and planetary magnetic pressure with an error no greater than 1%. We also discuss the contribution of hot plasma pressure and equatorial ring currents and their effects on magnetopause morphology. For each optimized magnetopause boundary, we give coefficients for fitted polynomial approximations to allow simple and accurate reproductions for practical applications. We specifically discuss the potential application to the modeling of Saturn's magnetopause and describe how the equilibrium magnetopause model can be used to estimate the compressibility of the boundary.

1. Introduction

The magnetopause is the boundary enclosing the magnetosphere of a magnetized body which separates it from the solar wind plasma. Its structure is inherently described by the interaction between the incident solar wind and internal pressure sources linked to the planetary magnetic and plasma environment.

The shape of this magnetic envelope is difficult to predict, as the detailed magnetic configuration close to a planet stems from an interplay of both internal and external magnetic fields and charged particles. Local or external sources of plasma, for example, may lead to magnetic contributions comparable to those of fields generated in the planet's interior or of solar origin. Thus, not only is the magnetopause surface system-dependent, it is also continuously accelerated due to the highly dynamic nature of these local pressure sources (Kaufmann & Konradi, 1969; Escoubet et al., 2013, 2015).

This dynamical behavior is largely governed by the magnetosphere trying to establish an equilibrium, or balance, between the internal and external sources of pressure. A *static* magnetopause surface at exact pressure balance could be considered as a good approximation of the boundary during "quiet times." Predicting its shape would help in understanding the general behavior of the magnetopause, as well as its local structure and dynamics under different regimes of exterior/interior pressure. It could also be a powerful tool for auroral studies and solar wind pressure estimation.

A self-consistent model for such an equilibrium magnetopause was first developed by Mead and Beard (1964): Using a dipolar planetary field, the pressure balance in this study was solved, moving radially from the subsolar nose and using a mix of discretization and extrapolation methods. The surface was then corrected by iterative computations of the shielding field associated with the magnetopause surface currents. Since then, several studies have aimed at determining the equilibrium surface under the introduction of diverse current systems (Maurice & Engle, 1995; Sotirelis & Meng, 1999; Zaharia et al., 2004).

Observations from the Saturn orbiter *Cassini* have recently motivated more empirical studies and modeling approaches of a planetary magnetopause. In the absence of an upstream solar-wind monitor, observed magnetopause crossings were used to model the shape of the boundary including variable solar wind pressure (Arridge et al., 2006; Kanani et al., 2010) and the behavior of the surface in response to variations in the internal plasma pressure distributions (Achilleos et al., 2010; Pilkington et al., 2014; Sorba et al., 2017). This latter effect was shown to have significant large-scale effects on the size and shape of Saturn's magnetopause (Pilkington et al., 2015).

This work describes the first steps toward a new numerical framework aiming at delivering a comprehensive theoretical model of Saturn's magnetopause. It is based on a modern take on self-consistent methods while also making use of the recent work and models developed using the data from the Cassini mission. The outlined method introduces new ways to account for different magnetic and pressure contributions—such as pressure resulting from hot plasma sources or the interplanetary magnetic field (IMF)—and presents efficient ways to compute, visualize, and assess equilibrium magnetopause boundaries.

Section 2 will define the magnetopause using the criterion of local pressure balance before introducing our numerical scheme. Section 3 will then describe how an equilibrium, field-dominated surface can be obtained using an *initial guess surface* which is constrained by specific profiles in the equatorial and noon-midnight meridian planes. Finally, in section 4, we will discuss potential future applications to Saturn's magnetopause by considering the separate introductions of hot plasma pressure and equatorial ring currents in the model.

2. Magnetopause Definition Using Local Pressure Balance

2.1. Local Solar Wind-Planetary Field Interactions

At Earth, the shape of the magnetopause boundary is mainly governed by the local pressure balance between the solar wind ram pressure and the magnetic pressure due to the dipole-like contribution of the intrinsic planetary field. This is not always the case in the vicinity of the gas giants Saturn and Jupiter, since their magnetospheres are strongly influenced by significant internal plasma populations. The corresponding additional plasma pressure has been shown to displace the magnetopause by up to 10–15 planetary radii at constant solar wind dynamic pressure for the case of Saturn (Pilkington et al., 2015). In a plasma-depleted state in which the magnetosphere is compressed toward the planet, however, the planetary contribution to the interior field may dominate (Arridge et al., 2008; Sorba et al., 2017). The magnetopause boundary would then be described by interactions similar to that of the Earth.

This section will study magnetopause equilibrium by focusing on the interior contribution of the planetary magnetic field. Further account for internal plasma pressure distribution, for example, will be considered in the rest of the paper and future work. In the next section, we will explain how this method can be adapted to describe more complete interactions.

Let us start by considering the following pressure balance equation

$$\rho v_{\perp}^2 = \frac{B_{\mathrm{tot}\parallel}^2}{2\mu_0}, \tag{1}$$

where ρ denotes the solar wind mass density, and $v_{\perp}$ the locally normal component of the solar wind velocity vector v onto the magnetopause surface. On the right-hand side, μ_0 is the vacuum permeability and $B_{\mathrm{tot}\parallel}$ is the tangential component of the total interior magnetic field B_{tot} at the boundary. This local equation implicitly defines the morphology of the equilibrium magnetopause surface.

By introducing the unit vector $\hat{\boldsymbol{n}}$ locally normal to the surface and pointing outward, this relation can be written as

$$2\mu_0\rho(\boldsymbol{v}\cdot\hat{\boldsymbol{n}})^2 = \left\|\hat{\boldsymbol{n}}\wedge\boldsymbol{B}_{\mathrm{tot}}\right\|^2. \tag{2}$$

A comparison of the validity of this pressure balance equation with the one from Petrinec and Russell (1997) can be found in section A.1. The total internal magnetic field B_{tot} may be expressed as (Mead & Beard, 1964)

$$\boldsymbol{B}_{\mathrm{tot}} = \boldsymbol{B}_{\mathrm{planet}} + \boldsymbol{B}_{\mathrm{fringing}}, \tag{3}$$

where

- B_{planet} is the intrinsic magnetic field of the planet.
- B_{fringing} denotes the shielding field produced by the currents flowing onto the surface consistent with the discontinuity of the parallel component of the field at the boundary. It can be expressed as the sum of a surface current planar field B_{p} and a curvature field B_{c}, leading to

$$\boldsymbol{B}_{\mathrm{tot}} = \boldsymbol{B}_{\mathrm{planet}} + \boldsymbol{B}_{\mathrm{p}} + \boldsymbol{B}_{\mathrm{c}}. \tag{4}$$

Similarly to Mead and Beard (1964), assuming an infinitesimally thin surface boundary, the field just outside of the magnetopause can then be considered as

$$\boldsymbol{B}_{\text{out}} = \boldsymbol{B}_{\text{planet}} + \boldsymbol{B}_{\text{c}} - \boldsymbol{B}_{\text{p}} = \boldsymbol{B}_{\text{IMF}}, \tag{5}$$

with B_{IMF} being the interplanetary field. Using equations (4) and (5), the total interior field can be expressed as

$$\boldsymbol{B}_{\text{tot}} = 2\left(\boldsymbol{B}_{\text{planet}} + \boldsymbol{B}_{\text{c}}\right) - \boldsymbol{B}_{\text{IMF}}. \tag{6}$$

This equation differs from Mead and Beard's (1964) in its inclusion of the IMF B_{IMF}, as there was a paucity of IMF data in the 1960s, in the early days of the Mariner program.

Assuming a typical value of $B_{\text{IMF}} \approx 1$ nT at Saturn, the contribution of the interplanetary field might initially be considered negligible when compared to the incident solar wind pressure. At points where the boundary is practically tangential to the solar wind flow, however, it may lead to a measurable effect on the shape of the surface. Such introduction of the IMF in the pressure balance will be considered in future work, but it has been neglected in this study.

Additionally, the curvature field B_{c} can be computed iteratively starting from a first optimized surface, as described by Mead and Beard (1964). Though its contribution can lead to a potentially useful model for the total interior field by canceling the normal component to the surface, its influence on the position of the magnetopause boundary has been shown to not be particularly significant (Mead & Beard, 1964). In this first step, we thus consider $B_{\text{c}} = \mathbf{0}$; this remains a reasonable approach since we consider the tangential component of the internal field in the initial pressure balance described by equation (1). The full contribution of the fringing field will be introduced in future work and is discussed in section 4.3.

These considerations lead to

$$2\mu_0\rho(\boldsymbol{v}\cdot\hat{\boldsymbol{n}})^2 = 4\left\|\hat{\boldsymbol{n}}\wedge\boldsymbol{B}_{\text{planet}}\right\|^2; \tag{7}$$

let us introduce the following scaling factors:

- a magnetic scaling factor

$$b_0 = \sqrt{2\mu_0\rho v^2}; \tag{8}$$

- a unit of distance

$$r_0 = R_p\left(\frac{2B_{\text{equ}}^2}{\mu_0\rho v^2}\right)^{\frac{1}{6}}, \tag{9}$$

corresponding to the location of the subsolar point. B_{equ} and R_p denote the planet's equatorial surface field and radius, respectively.

By dividing both sides of equation (7) by b_0, the balance between the solar wind dynamic pressure and the magnetic pressure at the magnetopause boundary can be described by the dimensionless equation

$$\left\|\hat{\boldsymbol{n}}\wedge\boldsymbol{B}^*_{\text{planet}}\right\| - \left(-\frac{1}{2}\hat{\boldsymbol{n}}\cdot\hat{\boldsymbol{v}}\right) = 0, \tag{10}$$

where the hat symbol indicates unit vectors, and the asterisk normalized variables. As illustrated in Figure 1, the solar wind velocity vector v is chosen to be normal to the planetary magnetic moment, in the opposite direction of the Z axis. Detailed expressions for the vectors can be found in section A.2.

From this point on, unless stated otherwise, we will work with the dimensionless pressure balance equation, equation (10), and the hat and asterisk symbols will be omitted. The term on the left of the minus sign corresponds to a scaled magnetic pressure, and the term in brackets linked to a scaled solar wind dynamic pressure. The following subsection describes how this pressure balance equation can be solved numerically using the method of finite differences.

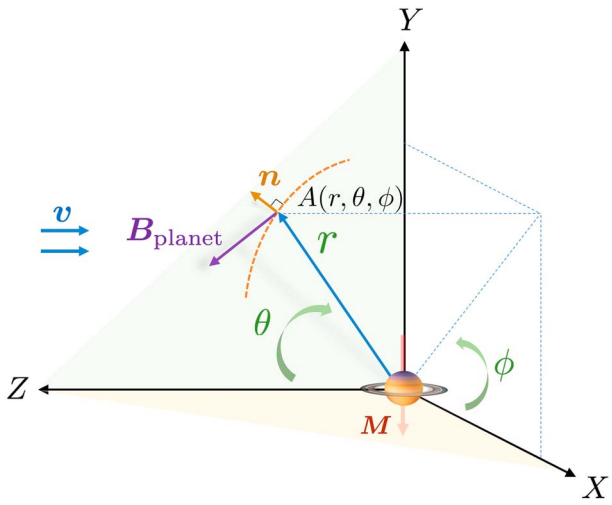

Figure 1. Cartoon illustrating the spherical coordinate system (r, θ, ϕ) used to locate a point on the magnetopause surface. The red arrow M represents the magnetic moment of the planet and points in the negative Y direction; the Z axis points toward the Sun, and the X axis completes the coordinate system.

2.2. Discretized Problem and Finite-Difference Approach

Using the spherical coordinates (r, θ, ϕ) illustrated in Figure 1, the pressure balance described in equation (10) is discretized on the two-dimensional $\theta \times \phi$ grid shown in Figure 2. On every point of this grid, we now wish to find the radial distance r at which the solar wind dynamic pressure balances the planetary magnetic pressure.

This two-dimensional grid can be remapped into a long one-dimensional array in order to identify each point of the grid by a single integer index k (see section A.3 for more details). The partial derivatives can now be approximated using centered finite differences as follows: At a point of the grid designated by an integer k,

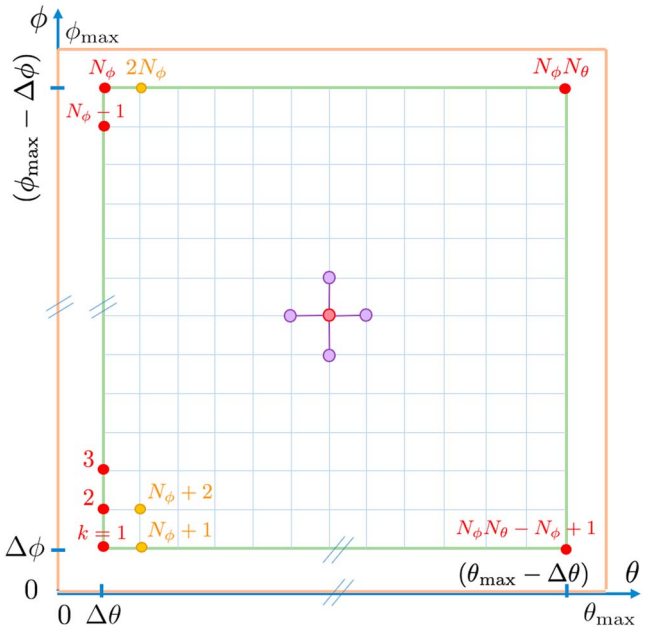

Figure 2. Cartoon of the two-dimensional grid on which a finite-difference scheme for equation (10) is expressed; the five-point stencil is illustrated by the "cross" in the center of the grid. θ_{max} and ϕ_{max} were chosen to be 120° and 90°, respectively, and $\Delta\theta = \Delta\phi = 0.5°$. The spherical coordinates r, θ, and ϕ are the ones illustrated on Figure 1. Several values of the single index k are shown in red and orange to depict the mapping between the 2-D and 1-D grids.

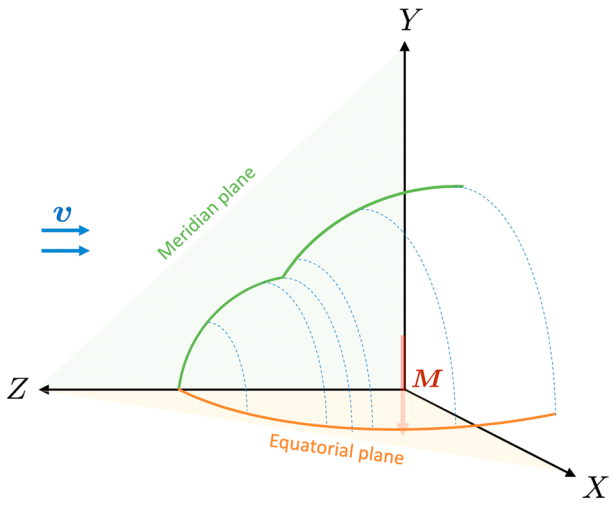

Figure 3. Cartoon depicting the construction of the initial guess surface using solutions in the equatorial (orange curve) and noon-midnight meridian (green curve) planes. The blue dotted lines indicate the elliptical cross sections, the red arrow the planetary magnetic moment, and v the solar wind flow. The "quadrant" of surface shown above is used to construct the full initial guess by assuming north-south and dawn-dusk symmetries.

$$\left(\frac{\partial r}{\partial \theta}\right) = \frac{r(k+N_\phi) - r(k-N_\phi)}{2\Delta\theta} + \mathcal{O}(\Delta\theta)^2, \tag{11}$$

$$\left(\frac{\partial r}{\partial \phi}\right) = \frac{r(k+1) - r(k-1)}{2\Delta\phi} + \mathcal{O}(\Delta\phi)^2, \tag{12}$$

where N_ϕ is the maximum extension of the corresponding 2-D grid in the ϕ direction. Equivalently, N_θ will be used to describe the maximum extension of the grid in the θ direction.

Using these finite difference approximations in equations (A6)–(A8), equation (10) can now be expressed as a set of algebraic pressure balance relations ($\mathcal{F}_k$), one for each point of the grid: $\forall k \in [1; N_\theta N_\phi]$,

$$\mathcal{F}_k\left(r_k, r_{k+N_\phi}, r_{k-N_\phi}, r_{k+1}, r_{k-1}, \theta_k, \phi_k\right) = 0. \tag{13}$$

The specific expressions of each function $\mathcal{F}_k$ will depend on whether point k describes a point interior to the grid, or in contact with one of its boundaries (see section A.3 for more details).

The discretized equilibrium magnetopause surface is now defined on the grid by the position vector solution of the equation

$$\boldsymbol{\mathcal{F}}(\mathbf{r}) = \mathbf{0}, \tag{14}$$

where $\boldsymbol{\mathcal{F}} = (\mathcal{F}_k)$ is the vector of local pressure balance relations on the grid and $\mathbf{r} = (r_k)$ the vector of radial position coordinates for points on the model magnetopause boundary.

The equilibrium surface can be found by solving equation (14) using numerical iterative methods: Starting from an initial guess surface, the boundary is refined at every iteration by stepping in a direction inspired by the Jacobian matrix $J_{\mathcal{F}}$ (see section A.4 for more details), until it converges to the final equilibrium surface.

2.3. Construction of the Initial Guess Surface

The construction of the initial guess surface is illustrated in Figure 3 and relies on three steps:

1. In the equatorial plane, the pressure balance equation, equation (10), is solved explicitly starting from the subsolar nose. Note that the pressure balance is exactly satisfied at the nose, through correct choice of the stand-off distance.
2. We consider the noon-midnight meridian plane as the top boundary of the grid: This allows us to make use of the inherent local symmetry of the magnetopause boundary and thus significantly reduces the dimension of the problem. Additionally, this helps to prevent the characteristic singular structure of the

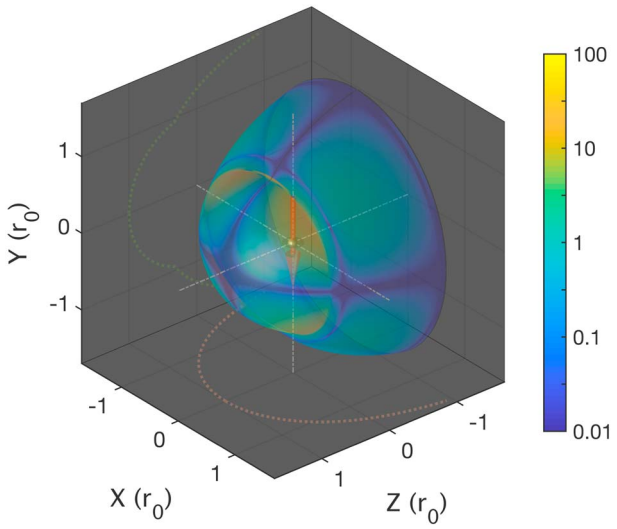

Figure 4. Relative error from exact pressure balance on the initial guess surface: The color bar indicates the percentage error using the indicator $|\Delta P| \,/\, |\langle P \rangle|$ defined in equation (15). The axes are scaled to the stand-off distance r_0 defined in equation (9). The planet is at the origin of the plot, the arrow indicating its magnetic moment. The bottom and top boundaries—equatorial and noon-midnight meridian solutions, respectively—are illustrated by the orange and green dotted curves projected onto the bottom and left planes. The cusp in the noon-midnight meridian plane leads to a "joint" where the initial error peaks at around $\approx 50\%$.

surface close to the polar cusp. The position of the polar cusp was determined accurately by considering the intersection of two branch solutions: one resulting from satisfying the pressure balance equation starting from the subsolar nose and the other obtained similarly starting from the point on the surface just above the planetary north pole. The method is briefly explained in section A.5 and will be detailed in future work.

3. Finally, these two solution curves are used to generate elliptical cross sections for fixed values of θ; this procedure thus results in a quarter of a three-dimensional initial magnetopause guess. Along the equatorial and noon-midnight profiles, we are making use of the surface symmetry by assuming $\frac{\partial r}{\partial \phi} = 0$.

The full initial magnetopause guess surface is found after imposing consecutive north-south and dawn-dusk symmetries. That surface is then iteratively adjusted to approach the local pressure balance at every point, until it converges to the final equilibrium boundary.

3. A Dipole-Dominated Magnetopause

3.1. Analysis of the Initial Guess Surface

In order to evaluate the accuracy of the initial equilibrium magnetopause surface, we consider the local value of the relative error defined by the ratio of the pressure difference ΔP between the interior and exterior, to the local mean pressure $\langle P \rangle$: At a point k of the grid, the relative error then corresponds to

$$\left| \frac{\Delta P}{\langle P \rangle} \right| (k), \tag{15}$$

where $\Delta P = \left(\left\| \hat{\boldsymbol{n}} \wedge \boldsymbol{B}^*_{\text{planet}} \right\| - \left(-\frac{1}{2} \hat{\boldsymbol{n}} \cdot \hat{\boldsymbol{v}} \right) \right)$ denotes the local discretized pressure balance residual of equation (13); $\langle P \rangle = \frac{1}{2} \left(\left\| \hat{\boldsymbol{n}} \wedge \boldsymbol{B}^*_{\text{planet}} \right\| + \left(-\frac{1}{2} \hat{\boldsymbol{n}} \cdot \hat{\boldsymbol{v}} \right) \right)$ is the local average value of the solar wind and magnetic pressure on each side of the boundary. The choice of using this estimate to assess the accuracy of the surface differs from previous studies: Mead and Beard (1964), for example, considered how small the exterior field was compared to the dipole field, or how tangential to the surface the interior field became after introduction of the shielding field. The method we have described is extremely useful to visualize how well each section of the surface quantitatively satisfies the pressure balance.

The relative error $|\Delta P| \,/\, |\langle P \rangle|$ on the initial guess surface is illustrated in Figure 4. By construction, the surface already satisfies the pressure balance to a satisfactory precision around the subsolar nose area and the equatorial and noon-midnight meridian planes.

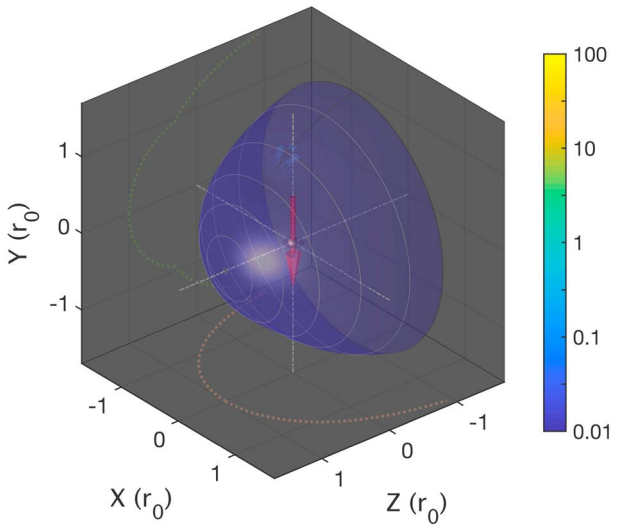

Figure 5. Relative error from exact pressure balance on the optimized magnetopause surface: The color bar indicates the percentage of error using the indicator $|\Delta P| \,/\, |\langle P \rangle|$) defined in equation (15); the black lines represent cross sections of the surface with planes of constant Z values. The axes are scaled to the stand-off distance r_0 defined in equation (9). The planet is at the origin of the plot, the arrow indicating its magnetic moment. The bottom and top boundaries—equatorial and noon-midnight meridian solutions, respectively—are illustrated by the orange and green dotted curves projected onto the bottom and left planes. Some iso-θ contours are shown in white on the surface.

There are four regions on the dayside in which the initial-guess boundary does not describe the pressure balance accurately, with a relative error close to $\approx 50\%$. This is partly explained by the fact that these regions intercept a comparatively small dynamic pressure from the solar wind flow due to the local curvature of the surface, leading to small values of the mean pressure $\langle P \rangle$. They extend to a value of θ which corresponds to the position of the cusp in the noon-midnight meridian plane.

We can then distinguish between two sections of the magnetopause surface: one section on the dayside extending from the subsolar nose to the θ value of the polar cusp, where the relative error goes up to $\approx 50\%$, and another "downstream" section corresponding to the rest of the surface, in which the initial percentage error is of the order of the unity. These two sections will be respectively named the *dayside cap* and the *tail region*.

3.2. Optimization Toward Pressure Balance

In order to reduce the size of the optimization problem and mitigate any error propagation in the derivative approximations due to the singular nature of the polar cusp, the optimization of the initial guess surface was done in three steps:

1. The magnetopause initial guess surface was *cut* at the θ value of the cusp to separate the dayside cap from the tail region. The dayside cap was first adjusted to satisfy the local pressure balance at every point using a Levenberg-Marquardt method (see section A.4 for more details).
2. The tail region was then corrected in the same way using the previous optimized surface to define its left boundary, the downstream boundary of the cusp being used as the upstream boundary of the tail.
3. The two optimized sections were finally merged back together to form a final optimized equilibrium boundary.

Using the Jacobian matrix (based on finite differences) defined in section A.4, the total optimization process converges to a final equilibrium surface in 20 or so iterations. This occurs when the values of the residuals on the surface become satisfyingly small; the stopping criterion is arbitrarily chosen as $\|\mathscr{F}(\mathbf{r})\|_2 < 10^{-5}$ where $\mathscr{F}(\mathbf{r})$ is defined in equation (14) and $\|.\|_2$ is the Euclidean L_2-norm.

3.3. Analysis of the Final Optimized Boundary

The local relative error from exact pressure balance on the final optimized surface is shown in Figure 5. We can see that the adjustment of the initial surface was very efficient: At almost every point of the magnetopause boundary, the difference between the solar wind dynamic pressure and the magnetic pressure does

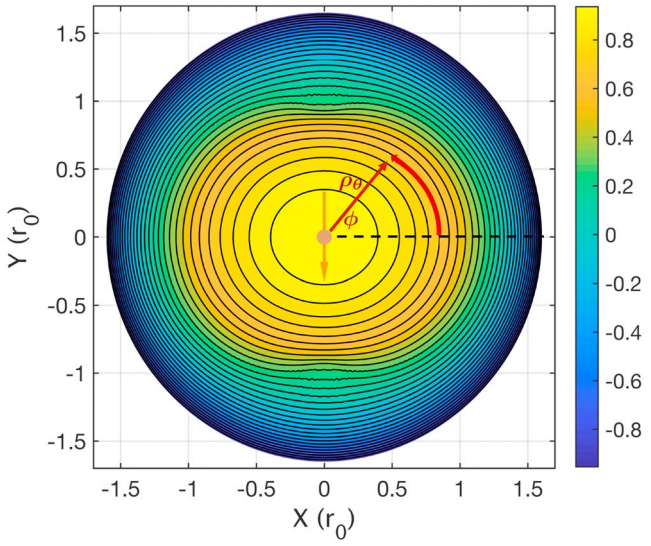

Figure 6. View of the equilibrium magnetopause surface from the Sun, each curve representing the cross section of the boundary at constant values of θ. $\rho_\theta(\phi)$ is the polar description of each curve corresponding to equation (16). The planet is at the origin of the plot, the arrow indicating its magnetic moment. The color bar indicates the "depth" of the surface—its position along the Z axis.

not exceed 1% of the local mean pressure. In particular, the method was particularly effective at correcting the region on the dayside where the relative error was initially quite high (see Figure 4). Some numerical artifacts can be seen on the final surface close to the polar cusp, but the corresponding numerical "jitter" remains negligible when compared to the local curvature of the boundary.

In order to allow a simple and accurate construction of the equilibrium magnetopause surface, we performed a least squares fit of polynomial descriptions for cross sections of the first quadrant of the optimized surface at constant θ. Looking at the planet from the position of the Sun, these curves, shown in Figure 6, can be described by the radial distance from the Z axis $\rho_\theta = r\sin\theta$; this distance is expressed as a fourth-order polynomial in ϕ

$$\rho_\theta = r\sin\theta = \sum_{k=0}^{4} a_{\theta,k}\,\phi^k\,, \tag{16}$$

where $\phi \in [0; \frac{\pi}{2}]$ is expressed in radians, and the values of the polynomial coefficients $a_{\theta,k}$ for different angular positions θ are given in Table A1. The full surface can be obtained by building the first quadrant using equation (16) and applying consecutive north-south and dawn-dusk symmetries.

4. Potential Applications and Refinements of the Model

4.1. Introduction of Interior Plasma Pressure

In order to assess in a simple way the effect of hot plasma pressure on the position of the magnetopause surface, let us refine the initial equation (1) by considering the following pressure balance relation

$$\rho v_\perp^2 = \frac{B_{\mathrm{tot}\|}^2}{2\mu_0}\,(1+\beta)\,, \tag{17}$$

where β is the local ratio of the hot plasma pressure to magnetic pressure.

This new equation is, in effect, equivalent to a problem governed by the initial pressure balance equation described in equation (1) where the initial stand-off distance r_0 of equation (9) is replaced by an effective value $(1+\beta)^{\frac{1}{6}} r_0$. Because the work in the previous section was done with distances being scaled to the position of the subsolar nose, the final equilibrium magnetopause boundary illustrated in Figure 5 is still applicable to equation (17).

The hot plasma pressure thus contributes to *inflating* the "zero-β" magnetopause surface by a factor of $(1+\beta)^{\frac{1}{6}}$. Using the initial expression for the stand-off distance r_0 given in equation (9), this corresponds to

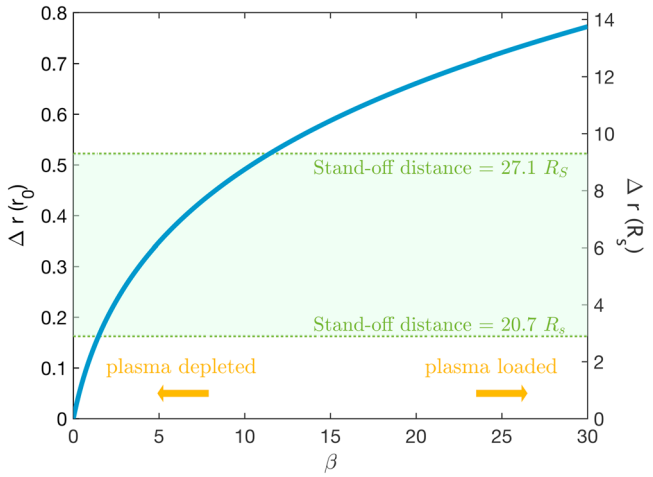

Figure 7. Inflation of Saturn's magnetopause due to hot plasma pressure as a function of plasma β—see equation (18). The left axis is expressed in units of r_0, which corresponds to the stand-off distance in the dipole dominated case defined in equation (9); the right axis is expressed in units of Saturn's radius R_s. The green dotted lines correspond to the means $20.7R_s$ and $27.1R_s$ for the bimodal distribution found by Pilkington et al. (2015) after fitting their model to magnetopause crossing data. Small values of beta correspond to a plasma depleted state, and high beta values correspond to a plasma loaded state in which the plasma pressure can dominate over the magnetic pressure.

a radial displacement Δr of the magnetopause boundary of

$$\Delta r = r_0 \left((1+\beta)^{\frac{1}{6}} - 1 \right) \approx 17.8 \quad R_s \left((1+\beta)^{\frac{1}{6}} - 1 \right), \tag{18}$$

for typical example values of the solar wind dynamic pressure and equatorial field for Saturn, R_s denoting the planetary radius. The inflation of the boundary Δr is plotted as a function of plasma β in Figure 7; for $\beta = 3$, for example, the magnetopause surface would be pushed outward by around 4.6 planetary radii. These simple considerations produce similar Δr values to the analogous observational and theoretical results of Pilkington et al. (2015) and Sorba et al. (2017) for the Kronian magnetopause, respectively.

4.2. Modeling the Contribution of Equatorial Ring Currents and Estimating Magnetopause Compressibility

At Saturn and Jupiter, the dynamics of the rapidly rotating magnetospheres are driven by internal sources of plasma from the planetary moons Enceladus and Io. The material ejected by these satellites is partially ionized, accelerated toward corotation with the ambient disk plasma, and confined toward the rotational equator by the centrifugal force. The resulting plasma sheet and currents distort the field into a "disk-like" structure known as a magnetodisk; it is characterized by field lines being stretched outward close to the equatorial plane and is supported by an azimuthal ring current. The activity of this ring current is enhanced by a population of hotter plasma originating from the outer magnetosphere (Sergis et al., 2007).

In order to model the position of a corresponding equilibrium magnetopause envelope, the local pressure balance thus needs to account for the contribution of the magnetic field produced by this azimuthal ring current. Work is currently being carried out to model the internal magnetodisk structure using Achilleos et al., 2010's (2010) force balance model. For the present purposes, this is done by superposing the dipolar (internal) planetary field and the field produced by a CAN-disk—in reference to Connerney, Acuña, Ness (Connerney et al., 1981, 1983)—to consider the following pressure balance relation

$$\rho v_\perp^2 = \frac{1}{2\mu_0} \left|\left| 2 \left(\boldsymbol{B}_{\text{planet}\parallel} + \boldsymbol{B}_{\text{disk}\parallel} \right) \right|\right|^2 (1+\beta), \tag{19}$$

where B_{planet} is the dipolar planetary field and B_{disk} models the contribution of the equatorial ring current, according to the formalism of the CAN model; the subscript $\parallel$ is used to denote the components of the field tangential to the surface. The inner and outer radii were fixed to $8R_s$ and $15.5R_s$, respectively, the disk half-thickness to $3R_s$ and $\mu_0 I_0$ to 60.4 nT (Connerney et al., 1983), R_s denoting the radius of Saturn.

Following the method described in sections 2 and 3, equation (19) was used to build the initial guess surface illustrated in Figure 8; the surface was then iteratively corrected until it converged to the equilibrium

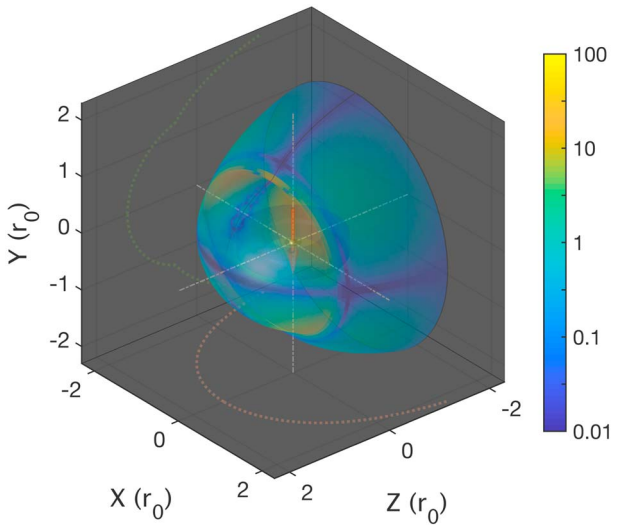

Figure 8. Relative error from the pressure balance described in equation (19) on the initial guess surface: The color bar indicates the percentage of error using the indicator $|\Delta P| / |\langle P \rangle|$ defined in equation (15). The axes are scaled to the stand-off distance r_0 in the dipole-dominated state, defined in equation (9). The planet is at the origin of the plot, the arrow indicating its magnetic moment. The bottom and top boundaries—equatorial and noon-midnight meridian solutions, respectively—are illustrated by the orange and green dotted curves projected onto the bottom and left planes. The CAN disk structure used to model the azimuthal current contribution is shown around the magnetic axis; the inner and outer radii were fixed to $8R_s$ and $15.5R_s$, the disk half-thickness to $3R_s$ and $\mu_0 I_0$ to 60.4 nT, with R_s denoting the radius of Saturn. CAN = Connerney, Acuña, Ness.

boundary shown in Figure 9. As with the dipole-dominated surface obtained in section 3.2, least squares fits of polynomial descriptions were performed for iso-θ cross sections: The first quadrant of the final equilibrium surface can be constructed using the polynomials in equation (16), with the corresponding coefficients listed in Table A2.

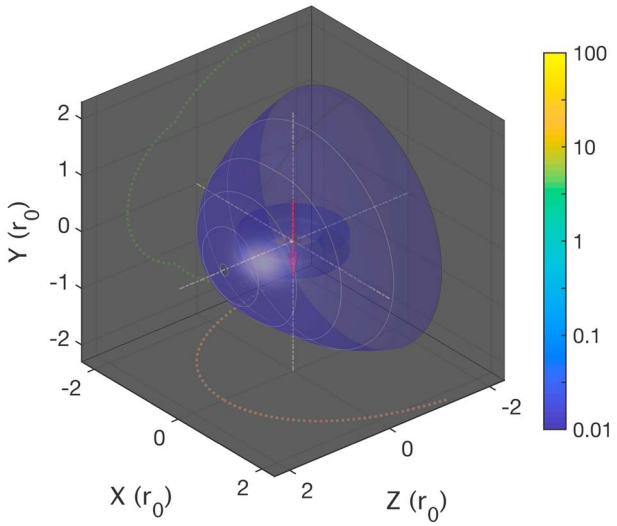

Figure 9. Relative error from the pressure balance described in equation (19) on the corrected surface: The color bar indicates the percentage of error using the indicator $|\Delta P| / |\langle P \rangle|$ defined in equation (15). The axes are scaled to the stand-off distance r_0 in the dipole-dominated state, defined in equation (9). The planet is at the origin of the plot, the arrow indicating its magnetic moment. The bottom and top boundaries—equatorial and noon-midnight meridian solutions, respectively—are illustrated by the orange and green dotted curves projected onto the bottom and left planes. The CAN disk structure used to model the azimuthal current contribution is shown around the magnetic axis; the parameters used are the same as the ones of Figure 8. CAN = Connerney, Acuña, Ness.

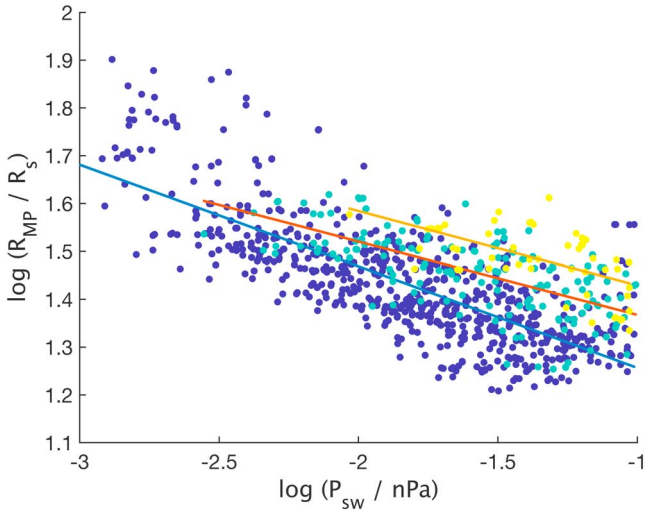

Figure 10. Determination of the compressibility parameter α using observed magnetopause crossings of the *Cassini* spacecraft and the relationship $R_{MP} \propto P_{sw}^{-1/\alpha}$, R_{MP} and P_{sw} denoting the stand-off distance and solar wind pressure, respectively. The crossings have been clustered in three groups using a k-clustering algorithm, depending on their local values of plasma β: $0 \leq \beta \leq 2.41$ in the dark blue cluster, $2.43 \leq \beta \leq 6.67$ in the green-blue cluster, and $6.69 \leq \beta \leq 14.45$ in the yellow cluster. The average compressibility parameter is found to be $\alpha \approx 5.2$.

Using the final equilibrium surface found in section 3 corresponding to a dipole-dominated case, we can estimate the equatorial "inflation" of the boundary due to the CAN disk: The terminator has been displaced by a distance $\Delta r_0 \approx 0.38\, r_0$, with r_0 denoting the value of the stand-off distance in the purely dipolar case defined in equation (9). Similarly, the positions of the boundary along the X axis and Y axis have been displaced by a distance of $\Delta r_{0X} \approx 0.37\, r_{0X}$ and $\Delta r_{0Y} \approx 0.32\, r_{0Y}$, r_{0X} and r_{0Y} being the positions of the magnetopause along the X and Y axes in the dipole-dominated case, respectively. The CAN disk has then led to an inflation of the boundary by approximately 37% and 38% along the X and Z axes in the equatorial plane and an inflation of around 32% along the Y axis in the noon-midnight meridian plane.

It is also possible to assess the effect of the modeled ring currents on how "compressed" the magnetopause is along the Y direction: The value of the flattening parameter $\epsilon = \frac{r_{0Y}}{r_{0X}}$ drops from 0.93 in the purely dipolar case (corresponding to a flattening of $\approx$ 7%) to 0.90 with the modeled magnetodisk structure (flattening of $\approx$ 10%). This is consistent with Pilkington et al., 2014's (2014) treatment of in situ data obtained by the Cassini spacecraft between 2007 and 2009, which indicates that the magnetopause boundary at Saturn is best described by a flattened surface along the north-south direction. The value of the surface flattening found by Pilkington et al. (2014) is, however, larger by a factor of 2—around $\approx$ 20%. This value corresponds to a simple dilation to an axisymmetric magnetopause boundary along the north-south direction: Due to the high concentration of low-latitude crossings in the data set, and since a compressed boundary cannot describe the "flaring" of the surface downstream from the cusp, it seems reasonable that we obtain a larger value for the flattening parameter ϵ. Just upstream from the cusp, for example, the flattening parameter takes a value of $\epsilon \approx 0.81$: This corresponds to a flattening of the boundary of $\approx$ 19% and is consistent with Pilkington et al., 2014's (2014) treatment of Cassini data.

Now that the effects of internal plasma activity have been introduced in the model, the equilibrium surfaces can also be used to estimate the compressibility of the magnetopause boundary at Saturn. The procedure can be summarized as follows:

- Magnetopause crossings of the Cassini spacecraft are identified using the Electron Spectrometer sensor of the Cassini Plasma Spectrometer instruments (Pilkington et al., 2015).
- At each crossing, measurements of the magnetic field strength and plasma activity are used alongside an equilibrium magnetopause surface to estimate the local solar wind pressure P_{sw}.
- Equilibrium boundaries are computed to "pass through" each crossing in order to estimate the corresponding stand-off distances R_{MP}.
- The compressibility parameter α is considered to link the magnetospheric scale to the solar wind pressure according to $R_{MP} \propto P_{sw}^{-1/\alpha}$; a plot of $\log R_{MP}$ with respect to $\log P_{sw}$ is shown in Figure 10, with the crossings being clustered depending on their values of plasma β. The average compressibility is found to be $\alpha \approx 5.2$.
- In order to assess this value of the compressibility and visualize the corresponding response of the magnetopause boundary to changes in solar wind pressure, the magnetopause crossings can be scaled to a reference pressure P_{ref} by considering the scaled crossing positions

$$\boldsymbol{OM}_{scaled} = \boldsymbol{OM}_{observed} \left(\frac{P_{ref}}{P_{sw}} \right)^{-1/\alpha}. \tag{20}$$

The results are shown in Figure 11: most of the scaled crossings are seen to cluster around the equilibrium surface, which seems to illustrate the validity of both the model—at least for a large part of the dayside magnetopause—and its application to determining the compressibility at Saturn.

4.3. Toward the Computation of the Induced Shielding Field

The final equilibrium magnetopause boundary can be used to compute the shielding field induced by currents flowing onto the surface. Because the initial pressure balance equation already considers the tangential

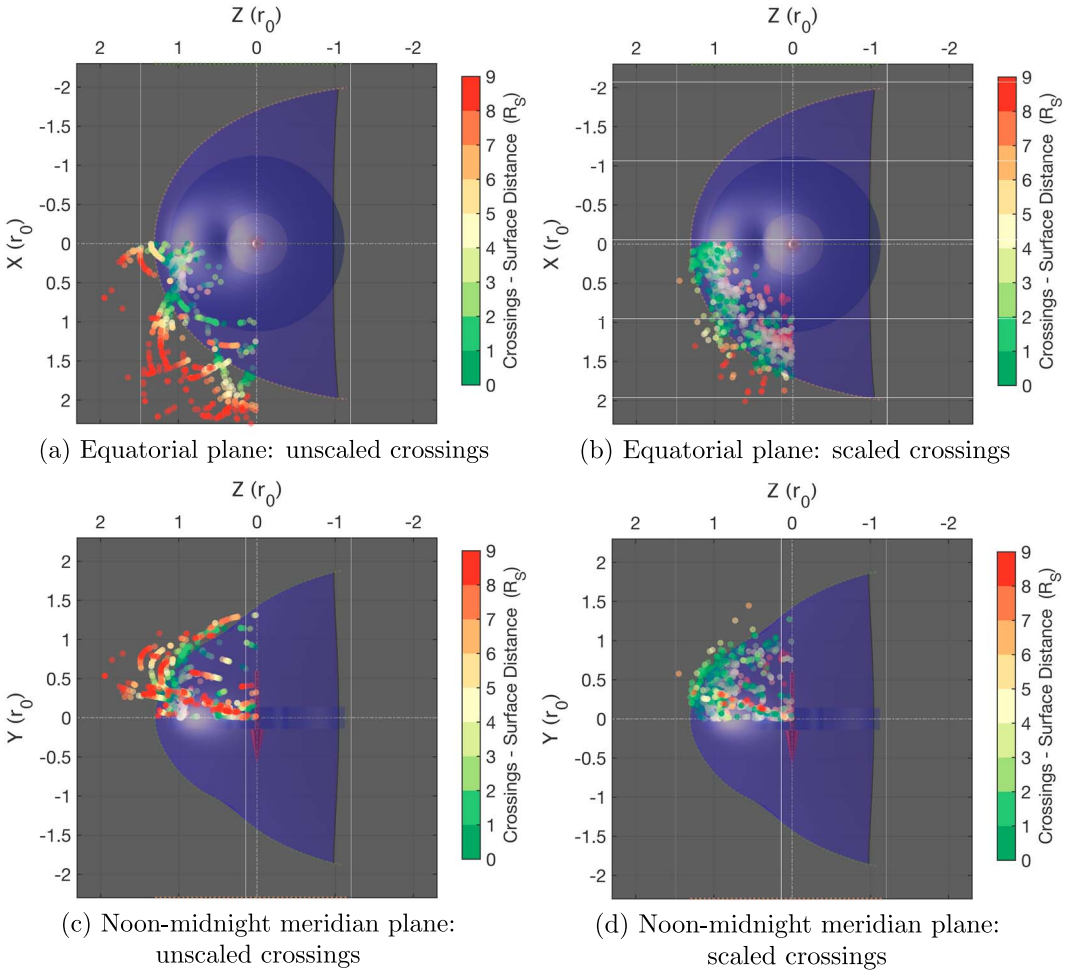

Figure 11. Distances of nonscaled (a and c) and scaled (b and d) crossings from an equilibrium magnetopause surface. The degree of scatter is similar to the residuals found when fitting purely empirical models (Arridge et al., 2006; Pilkington et al., 2015). All the crossings with local plasma β inferior to 15 were kept.

component of the interior field, the additional contribution of this magnetic field would only lead to small corrections in the local magnetopause morphology, as shown by Mead and Beard (1964). However, introducing the shielding field would prove useful in correcting the interior field by canceling its normal component to the boundary, thus leading to a model for the magnetospheric field consistent with the equilibrium magnetopause surface. The contribution of the shielding field will be presented in future work, but preliminary studies show that its effect accounts for a displacement of the subsolar nose of the order of 10%.

5. Conclusion

The method described in this paper can be used to construct an equilibrium magnetopause boundary on which the external and internal pressure sources are balanced. We explain how the local pressure balance can be used to define the steady-state magnetopause as the solution of an optimization problem. We detail the construction of an initial nonaxisymmetric boundary using solutions of the pressure balance at the subsolar nose and along the equatorial and noon-midnight meridian planes.

A numerical scheme is implemented to correct the initial surface and obtain a final optimized magnetopause surface that satisfies pressure equilibrium with a relative error inferior to 1%. In particular, the final boundary allows a particularly novel and accurate description of the high-latitude structure close to the polar cusp.

We explain how the method can be refined with the introduction of hot plasma pressure and modeled contributions of azimuthal ring currents. When applied to Saturn, the model is then shown to be in concordance with results derived from Cassini magnetospheric data. We also describe how the equilibrium surfaces can be used alongside observed magnetopause crossings to estimate local values of solar wind pressure and the compressibility of the magnetopause boundary. Further refinements of the model—for example, the inclusion of an "efficiency" fraction for the IMF contribution to the interior magnetospheric field model (Alexeev & Belenkaya, 2005) and the modeling of the magnetopause oscillating effects due to corotating partial ring currents evidenced by many Cassini-ENA measurements (Krimigis et al., 2007)—will be considered. The method lends itself well to 3-D visualizations of the optimized surface morphology and its accuracy regarding exact pressure balance. Polynomial descriptions of surface contours are given to allow simple and accurate constructions of the entire magnetopause boundary.

Appendix A

A.1. Describing the Local Pressure Balance

The model described in this paper makes use of the pressure balance equation, equation (1), assuming perfect elastic specular reflection of solar wind particles. A more detailed formalism, which accounts for effects of magnetosheath plasma flow, could read (Petrinec & Russell, 1997)

$$P_{\text{ext}} = KP_{\text{sw}}\cos^2\psi + P_0\sin^2\psi = P_{\text{int}}\,, \tag{A1}$$

where ψ is the angle between the solar wind flow direction and the normal of the surface, P_0 the static thermal pressure, and K the coefficient accounting for the divergence of the incident magnetosheath flow. The additional P_0 term would only become important for values of ψ satisfying, for example,

$$P_0\sin^2\psi > 0.2\left(KP_{\text{sw}}\cos^2\psi\right)\,, \tag{A2}$$

leading to

$$\tan^2\psi > 0.2K\frac{P_{\text{sw}}}{P_0} \approx 0.2\frac{P_{\text{sw}}}{P_0}\,, \tag{A3}$$

K being of the order of unity. The pressure ratio P_{sw}/P_0 is approximately equal to the square of the upstream sonic Mach number at Saturn $M_S \approx 14$ (Achilleos et al., 2006; Masters et al., 2008), leading to a limiting value ψ_c

$$\psi_c \approx \tan^{-1}\left(14\sqrt{0.2}\right) \approx 81°\,. \tag{A4}$$

This corresponds to a position quite far downstream; the model described in this paper could thus be considered valid for a large portion of the dayside magnetopause.

A.2. Formal Definition of the Magnetopause Surface

Equation (10) allows us to define explicitly the magnetopause boundary through the local pressure balance: Using the spherical coordinates illustrated in Figure 1, the surface corresponds to the set of points $S = \{A(r,\theta,\phi) \in \mathbb{R}^3\}$ such that

$$\begin{gathered} F(r,\theta,\phi) = r - f(\theta,\phi) = 0\,, \\ \text{where} \quad f : [0;\pi[\times[0;2\pi[\to\mathbb{R} \quad | \quad \left\| \hat{\boldsymbol{n}}\wedge\boldsymbol{B}^*_{\text{planet}} \right\| + \frac{1}{2}\hat{\boldsymbol{n}}\cdot\hat{\boldsymbol{v}} = 0\,, \\ \text{with} \quad \hat{\boldsymbol{n}} = \frac{\nabla F}{\|\nabla F\|} = \frac{\hat{\boldsymbol{e}}_r - \nabla f}{\|\nabla\hat{\boldsymbol{e}}_r - \nabla f\|} \end{gathered} \tag{A5}$$

The vectors can be expressed in the same coordinate system as follows:

1. The unit outward vector $\hat{\boldsymbol{n}}$ locally normal to the surface is a scaled gradient

$$\hat{\boldsymbol{n}} = \frac{\left(\hat{\boldsymbol{e}}_r - \frac{1}{r}\frac{\partial f}{\partial\theta}\hat{\boldsymbol{e}}_{\boldsymbol{\theta}} - \frac{1}{r\sin\theta}\frac{\partial f}{\partial\phi}\hat{\boldsymbol{e}}_{\boldsymbol{\phi}}\right)}{\|\boldsymbol{n}\|} = \frac{\left(\hat{\boldsymbol{e}}_r - \frac{1}{r^*}\frac{\partial f^*}{\partial\theta}\hat{\boldsymbol{e}}_{\boldsymbol{\theta}} - \frac{1}{r^*\sin\theta}\frac{\partial f^*}{\partial\phi}\hat{\boldsymbol{e}}_{\boldsymbol{\phi}}\right)}{\|\boldsymbol{n}\|} \tag{A6}$$

with $r^* = f^*(\theta,\phi) = \frac{f(\theta,\phi)}{r_0} = \frac{r}{r_0}$, r_0 corresponding to the location of the subsolar point defined in equation (9).

2. $\boldsymbol{B}^*_{\text{planet}}$ is the scaled magnetic field of the planet; it is modeled by a dipolar field with its magnetic moment aligned with the Y axis (see Figure 1)

$$\boldsymbol{B}^*_{\text{planet}} = \frac{\boldsymbol{B}_{\text{planet}}}{b_0} = \frac{M^*}{r^{*3}}\left(-2\sin\theta\sin\phi\,\hat{\boldsymbol{e}}_{\boldsymbol{r}} + \cos\theta\sin\phi\,\hat{\boldsymbol{e}}_{\boldsymbol{\theta}} + \cos\phi\,\hat{\boldsymbol{e}}_{\boldsymbol{\phi}}\right), \tag{A7}$$

with $M^* = \frac{B_{\text{equ}}}{b_0}\left(\frac{R_p}{r_0}\right)^3$ playing the role of a normalized magnetic moment, B_{equ} and R_p denoting the planet's equatorial surface field and radius, respectively.

3. $\hat{\boldsymbol{v}}$ is the unit velocity vector of the incoming solar wind plasma stream

$$\hat{\boldsymbol{v}} = -\cos\theta\,\hat{\boldsymbol{e}}_{\boldsymbol{r}} + \sin\theta\,\hat{\boldsymbol{e}}_{\boldsymbol{\theta}}. \tag{A8}$$

A.3. Description of the Grid and Its Boundary Conditions

We distinguish between three distinct sets of points in Figure 2:

1. the *interior points* on the blue lines describing a N_θ by N_ϕ grid, where N_θ and N_ϕ denote the maximum extensions of the grid in the θ and ϕ directions. Every point on this interior grid is associated to its linear index k; as illustrated in Figure 2, this index can be defined using the Cartesian coordinates (j,i) on the following grid:

$$k = (j-1)N_\phi + i. \tag{A9}$$

2. the *boundary points* of the grid, on the green lines: These points, which define the limits of the grid, are the ones on which the boundary conditions of the orange lines will have a direct impact through the discretization of the differentiation operators.
3. the *outer points* surrounding the grid, on the orange lines: They are the points on which the boundary conditions are fixed, thus conditioning the optimization of the surface on the interior grid. Points on the *left boundary* of the grid correspond to the subsolar nose: $r = r(\theta = 0) = r_0 = 1$. The *bottom boundary* describes the equatorial plane $\phi = 0$: The values of the points are given by the equatorial solution mentioned in section 2.3. The *top boundary* was chosen to describe the noon-midnight meridian plane $\phi = \frac{\pi}{2}$; the curve solution found in that plane determines the values of the points on that boundary. Finally, the *right boundary* was defined as a linear extrapolation in the θ direction using the previous values of r on the following grid:

$$r(k) = 2 \quad r(k-N_\phi) - r(k-2N_\phi) \qquad \text{for k} \in [N_\phi N_\theta - N_\phi + 1, N_\phi N_\theta]. \tag{A10}$$

A.4. Optimization Method Using a Levenberg-Marquardt Method

The final equilibrium magnetopause surface is found by adjusting the initial guess surface described in section 2.3 toward external-internal pressure balance. This is done iteratively following a Levenberg-Marquardt method: At each step, the search direction is a cross between the Gauss-Newton direction and the steepest descent direction. The adjustment δr^k to the surface $\mathbf{r}^k$ at step k is considered to be the solution of

$$\left((J_{\mathscr{F}}(\mathbf{r}^k))^T J_{\mathscr{F}}(\mathbf{r}^k) + \lambda_k \mathcal{I}\right)\delta r^k = -(J_{\mathscr{F}}(\mathbf{r}^k))^T \mathscr{F}(\mathbf{r}^k), \tag{A11}$$

where $\mathscr{F} = (F_k)$ is the vector of local pressure balance relations on the grid introduced in equation (14); $\mathcal{I}$ is the identity matrix, and λ_k a damping parameter controlling both the norm and direction of the correction δr^k and adjusted at each iteration to ensure descent at every step. $\lambda_k = 0$ corresponds to a direction of δr^k identical to that of the Gauss-Newton method; this direction tends toward the steepest descent direction as λ_k tends to infinity.

$J_{\mathscr{F}}$ denotes the Jacobian matrix $\left(\frac{\partial F_i}{\partial r_j}\right)_{(i,j)}$, each index i and j ranging from 1 to $N_\phi N_\theta$. It was computed analytically before being evaluated at every step, which sped up the optimization of the surface significantly.

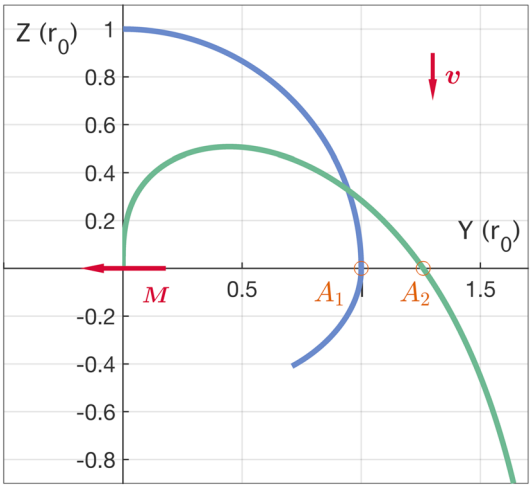

Figure A1. The two branch solutions found by integrating the pressure balance equation, equation (10), in the noon-midnight meridian plane, in the dipole-dominated case. The blue curve is the solution of an integration starting from the subsolar nose, defined in equation (9); A_1 is the point at which the branch crosses the Y axis locally parallel to the solar wind flow. The green branch is the solution of two consecutive integrations—upstream and downstream—starting from A_2. This point corresponds to the position at which the surface crosses the Y axis with a nonzero inclination. The overall profile is found by keeping the segments "facing" the solar wind flow, with the polar cusp corresponding to the intersection of both branches. r_0, v, and M denote the stand-off distance, the solar wind velocity vector, and planetary magnetic moment, respectively.

Given the expressions of each function F_i in equation (13), this matrix is sparse with only five nonzero subdiagonals:

$$J_{\mathcal{F}} = \begin{bmatrix} \frac{\partial F_1}{\partial r_1} & \frac{\partial F_1}{\partial r_2} & & & & \frac{\partial F_1}{\partial r_{N_\phi+1}} & & & & \\ \frac{\partial F_2}{\partial r_1} & \ddots & \ddots & & & & \ddots & & & \\ & \ddots & \ddots & \ddots & & & & \ddots & & \\ & & \ddots & \ddots & \ddots & & & & \frac{\partial F_{N_\phi N_\theta - N_\phi}}{\partial r_{N_\phi N_\theta}} & \\ & & & \ddots & \ddots & \ddots & & & & \\ \frac{\partial F_{N_\phi+1}}{\partial r_1} & & & & \ddots & \ddots & \ddots & & & \\ & \ddots & & & & \ddots & \ddots & \ddots & \frac{\partial F_{N_\phi N_\theta - 1}}{\partial r_{N_\phi N_\theta}} & \\ & & \frac{\partial F_{N_\phi N_\theta}}{\partial r_{N_\phi N_\theta - N_\phi}} & & & & \frac{\partial F_{N_\phi N_\theta}}{\partial r_{N_\phi N_\theta - 1}} & & \frac{\partial F_{N_\phi N_\theta}}{\partial r_{N_\phi N_\theta}} & \end{bmatrix} \tag{A12}$$

Table A1
Coefficients of the Radial Distance ρ_θ of Equation (16) Fitted to the Equilibrium Surface Corresponding to the Pure Dipole Case (See Section 3.3)

$\theta(^\circ)$	$a_{\theta,0}$	$a_{\theta,1}$	$a_{\theta,2}$	$a_{\theta,3}$	$a_{\theta,4}$
5	0.0872	0.0000	−0.0001	0.0000	0.0000
20	0.3464	0.0003	−0.0054	0.0019	0.0002
35	0.5968	0.0006	−0.0214	0.0017	0.0036
50	0.8325	−0.0049	−0.0239	−0.0325	0.0207
65	1.0488	−0.0245	0.0205	−0.1153	0.0475
70	1.1147	−0.0168	−0.0170	−0.0710	0.0268
75	1.1795	−0.0398	0.0615	−0.1686	0.0647
80	1.2396	−0.0364	0.0599	−0.1829	0.0783
100	1.4468	0.0113	−0.0872	0.0400	0.0010
120	1.6041	0.0074	−0.0043	0.0384	−0.0166

Table A2
Coefficients of the Radial Distance ρ_θ of Equation (16) Fitted to the Equilibrium Surface Modeling the Effect of Interior Plasma Pressure and the Contribution of Equatorial Ring Currents (See Section 4.2)

$\theta(^\circ)$	$a_{\theta,0}$	$a_{\theta,1}$	$a_{\theta,2}$	$a_{\theta,3}$	$a_{\theta,4}$
6	0.1450	0.0000	−0.0004	0.0002	0.0000
26	0.6201	0.0010	−0.0252	0.0087	0.0011
46	1.0656	−0.0004	−0.0863	0.0073	0.0144
66	1.4624	−0.0212	−0.0921	−0.0653	0.0426
70	1.5337	−0.0096	−0.1527	0.0047	0.0128
74	1.6041	−0.0326	−0.0714	−0.1095	0.0601
78	1.6710	−0.0409	−0.0399	−0.1625	0.0869
82	1.7341	−0.0289	−0.0815	−0.1218	0.0787
100	1.9825	0.0040	−0.1897	0.0818	0.0034
120	2.1888	0.0210	−0.1153	0.1059	−0.0267

A.5. Finding the Profiles in the Equatorial and Noon-Midnight Meridian Planes

The bottom and top boundaries of the grid are, respectively, fixed to $\phi = 0$ and $\phi = \frac{\pi}{2}$, corresponding to the equatorial and noon-midnight meridian planes. The pressure balance relation described in equation (10) can be solved along those planes by integrating it numerically from specific points of the magnetopause surface. The detailed method will be described in future work, but we present here its main points.

Specifically, in the equatorial plane, the starting point of the integration can be chosen as the subsolar nose, whose position along the Z axis is given by equation (9).

In the noon-midnight meridian plane, the structure close to the cusp can be solved by finding two branch solutions through three consecutive integrations:

- A first one starting from the subsolar nose, leading to the blue branch in Figure A1; this solution crosses the Y axis parallel to the solar wind flow at a point named A_1.
- A second integration can be carried out downstream, starting from the point A_2. The location of this point is found by determining analytically where the surface crosses the Y axis with a nonzero inclination.
- A third and last upstream integration starting from A_2 completes the green branch shown in Figure A1.

The final profile in the noon-midnight meridian plane—corresponding to the green curve shown in Figure 3, for example—is found by keeping the segments of the branches that "intercept" the solar wind flow; the polar cusp is found at the intersection of both branches.

A.6. Coefficients for Polynomial Fits to the Equilibrium Magnetopause Surfaces

As described in section 3.3, the optimized surfaces can be reproduced using equation (16), Figure 6, and the coefficients from Table A1 for the purely dipole case or Table A2 for additional contributions of interior plasma pressure and equatorial ring currents.

Acknowledgments
The authors wish to thank the reviewers for useful discussions, comments, and suggestions. F. H. was supported by a studentship jointly funded by UCL's Perren and Impact schemes. N. A. and P. G. were supported by the UK STFC Consolidated Grant (UCL/MSSL Solar and Planetary Physics, ST/N000722/1). The magnetopause crossings of the Cassini spacecraft mentioned in this study were identified by Pilkington et al. (2015) using the Cassini MAG, CAPS-ELS, and MIMI data available from the Planetary Data System (http://pds.nasa.gov/).

References

Achilleos, N., Bertucci, C., Russell, C. T., Hospodarsky, G. B., Rymer, A. M., Arridge, C. S., et al. (2006). Orientation, location, and velocity of Saturn's bow shock: Initial results from the Cassini spacecraft. *Journal of Geophysical Research*, *111*, A03201. https://doi.org/10.1029/2005JA011297

Achilleos, N., Guio, P., & Arridge, C. S. (2010). A model of force balance in Saturn's magnetodisc. *Monthly Notices of the Royal Astronomical Society*, *401*(4), 2349–2371. https://doi.org/10.1111/j.1365-2966.2009.15865.x

Alexeev, I. I., & Belenkaya, E. S. (2005). Modeling of the Jovian magnetosphere. *Annales Geophysicae*, *23*(3), 809–826. https://doi.org/10.5194/angeo-23-809-2005

Arridge, C. S., Achilleos, N., Dougherty, M. K., Khurana, K. K., & Russell, C. T. (2006). Modeling the size and shape of Saturn's magnetopause with variable dynamic pressure. *Journal of Geophysical Research*, *111*, A11227. https://doi.org/10.1029/2005JA011574

Arridge, C. S., Russell, C. T., Khurana, K. K., Achilleos, N., Cowley, S. W. H., Dougherty, M. K., et al. (2008). Saturn's magnetodisc current sheet. *Journal of Geophysical Research*, *113*, A04214. https://doi.org/10.1029/2007JA012540

Connerney, J. E. P., Acuña, M. H., & Ness, N. F. (1981). Modeling the Jovian current sheet and inner magnetosphere. *Journal of Geophysical Research*, *86*(A10), 8370–8384. https://doi.org/10.1029/JA086iA10p08370

Connerney, J. E. P. P., Acuna, M. H., Ness, N. F., Acuña, M. H., & Ness, N. F. (1983). Currents in Saturn'S magnetosphere. *Journal of Geophysical Research*, *88*(A11), 8779–8789. https://doi.org/10.1029/JA088iA11p08779

Escoubet, C. P., Masson, A., Laakso, H., & Goldstein, M. L. (2015). Recent highlights from Cluster, the first 3-D magnetospheric mission. *Annales Geophysicae*, *33*, 1221–1235. https://doi.org/10.5194/angeo-33-1221-2015

Escoubet, C. P., Taylor, M. G. G. T., Masson, A., Laakso, H., Volpp, J., Hapgood, M., & Goldstein, M. L. (2013). Dynamical processes in space: Cluster results. *Annales Geophysicae*, *31*, 1045–1059. https://doi.org/10.5194/angeo-31-1045-2013

Kanani, S. J., Arridge, C. S., Jones, G. H., Fazakerley, A. N., McAndrews, H. J., Sergis, N., et al. (2010). A new form of Saturn's magnetopause using a dynamic pressure balance model, based on in situ, multi-instrument Cassini measurements. *Journal of Geophysical Research*, *115*, A06207. https://doi.org/10.1029/2009JA014262

Kaufmann, R. L., & Konradi, A. (1969). Explorer 12 magnetopause observations: Large-scale nonuniform motion. *Journal of Geophysical Research*, *74*(14), 3609–3627. https://doi.org/10.1029/JA074i014p03609

Krimigis, S. M., Sergis, N., Mitchell, D. G., Hamilton, D. C., & Krupp, N. (2007). A dynamic, rotating ring current around Saturn. *Nature*, *450*, 1050–1053. https://doi.org/10.1038/nature06425

Masters, A., Achilleos, N., Dougherty, M. K., Slavin, J. A., Hospodarsky, G. B., Arridge, C. S., & Coates, A. J. (2008). An empirical model of Saturn's bow shock: Cassini observations of shock location and shape. *Journal of Geophysical Research*, *113*, A10210. https://doi.org/10.1029/2008JA013276

Maurice, S, & Engle, I. M. (1995). Idealized Saturn magnetosphere shape and field. *Journal of Geophysical Research*, *100*(A9), 17,143–17,151.

Mead, G. D., & Beard, D. B. (1964). Shape of the geomagnetic field solar wind boundary. *Journal of Geophysical Research*, *69*(7), 1169–1179. https://doi.org/10.1029/JZ069i007p01169

Petrinec, S. M., & Russell, C. T. (1997). Hydrodynamic and MHD equations across the bow shock and along the surfaces of planetary obstacles. *Space Science Reviews*, *79*(3/4), 757–791. https://doi.org/10.1023/A:1004938724300

Pilkington, N. M., Achilleos, N., Arridge, C. S., Guio, P., Masters, A., Ray, L. C., et al. (2015). Internally driven large-scale changes in the size of Saturn's magnetosphere. *Journal of Geophysical Research A: Space Physics*, *120*, 7289–7306. https://doi.org/10.1002/2015JA021290

Pilkington, N. M., Achilleos, N., Arridge, C. S., Masters, A., Sergis, N., Coates, A. J., & Dougherty, M. K. (2014). Polar confinement of Saturn's magnetosphere revealed by in situ Cassini observations. *Journal of Geophysical Research: Space Physics*, *119*, 2858–2875. https://doi.org/10.1002/2014JA019774

Sergis, N., Krimigis, S. M., Mitchell, D. G., Hamilton, D. C., Krupp, N., Mauk, B. M., et al. (2007). Ring current at Saturn: Energetic particle pressure in Saturn's equatorial magnetosphere measured with Cassini/MIMI. *Geophysical Research Letters*, *34*, L09102. https://doi.org/10.1029/2006GL029223

Sorba, A. M., Achilleos, N. A., Guio, P., Arridge, C. S., Pilkington, N. M., Masters, A., et al. (2017). Modeling the compressibility of Saturn's magnetosphere in response to internal and external influences. *Journal of Geophysical Research: Space Physics*, *122*, 1572–1589. https://doi.org/10.1002/2016JA023544

Sotirelis, Thomas, & Meng, Ching-I. (1999). Magnetopause from pressure balance. *Journal of Geophysical Research*, *104*(A4), 6889. https://doi.org/10.1029/1998JA900119

Zaharia, S., Cheng, C. Z., & Maezawa, K. (2004). 3-D force-balanced magnetospheric configurations. *Annales Geophysicae*, *22*(1), 251–265. https://doi.org/10.5194/angeo-22-251-2004